ChemComm

COMMUNICATION

View Article Online
View Journal | View Issue

In situ observation of electrolytic H_2 evolution adjacent to gold cathodes†

Cite this: *Chem. Commun.*, 2014, **50**, 1761

Received 3rd September 2013,
Accepted 16th December 2013

DOI: 10.1039/c3cc46737f

www.rsc.org/chemcomm

Y. Liu and S. J. Dillon*

The early stages of gas evolution during electrolytic hydrogen production on Au electrodes are characterized by *in situ* transmission electron microscopy. The results demonstrate that reaction product molecules initially dissolve into solution and then nucleate near, but not on, the electrodes. The gas subsequently wets the electrodes and its successive evolution is governed by triple phase boundary line motion.

As the cost of renewable energy sources approaches grid parity, the need for large-scale efficient energy storage and conversion becomes increasingly important. Electrolytic fuel production remains a leading candidate technology for accommodating excess load on the power grid. The resultant hydrogen may be used in fuel cells, generators, or transportation applications. The efficiency of the overall fuel cycle is sensitive to the overpotential associated with electrolysis. The current–overpotential relationship is sensitive to a number of parameters associated with the design and chemistry of the electrodes and electrolyte. Gas bubble nucleation, growth, and transport have long been recognized as important steps affecting the current–overpotential relationship. For example, they can block the electrode surface and inhibit the reaction, or promote mixing in the solution during detachment and enhance mass transport.[1]

The nucleation and growth of electrolytically generated gas has been the subject of numerous studies, most of which employ electrochemistry, optical microscopy or scanning probe microscopy.[2–7] The details of the process depend on solution chemistry, electrode chemistry, surface roughness, the type of gas evolved. The growth and motion of the bubbles depends on hydrodynamics, capillarity, and intermolecular force balances.[8] Generally, the reaction product molecules dissolve into solution until they supersaturate sufficiently to promote nucleation. The evolution of hydrogen gas from the supersaturated solution may be predicted based on classical nucleation theory. Dapkus and Sides[2] observed that nucleation occurs when the bulk concentration is $\sim 4\times$ the solubility limit. However, nucleation is localized to the electrode surface. Here the H_2 concentration may be 1- to 2-orders of magnitude larger than the bulk solubility.[2,7] Classical nucleation theory in absence of any field effects would predict supersaturation 3-orders of magnitude in excess of solubility. The discrepancy has been rationalized based on the assumption that homogeneous nucleation occurs in the electrical double-layer.[2] Here the electric field may reduce the water–gas surface energy, which lowers the nucleation barrier energy. Whether nucleation occurs homogeneously or heterogeneously will depend on geometry and the relative interfacial energies. The work by Dapkus and Sides characterized the reaction on mercury drop electrodes.[2] A number of recent studies employing scanning probe microscopy find that gas nuclei wet highly oriented pyrolytic graphite electrodes with small contact angles.[6] The system is ideal for scan probe microscopy and has relevance to carbonaceous catalyst supports. However, the interactions at these planar hydrophobic surfaces may differ significantly from those of metallic catalysts often employed for electrolysis.

Unfortunately, overall electrolytic gas evolution is still poorly understood as electrochemical techniques do not provide spatially resolved data, optical techniques do not probe sufficiently small length scales, and scan probe techniques lack temporal resolution and can not probe the bubble–electrode interface. This work seeks to characterize electrolytic gas production using *in situ* environmental transmission electron microscopy (TEM). The approach allows for high spatial resolution, reasonable temporal resolution, and probing of the bubble–solid interface.[9] *In situ* TEM suffers from projection effects, confinement of liquids inherent to producing thin samples, and potential electron beam effects. While the former two effects cannot be mitigated, electron beam effects may be minimized such that they are negligible relative to an appropriately large external stimulus. For example, several researchers[10] have noted that the electron beam current density may be reduced to the point where it generates no gas bubbles for extended periods of time. An external electric field may generate electrolytic

Department of Materials Science and Engineering, University of Illinois at Urbana-Champaign, 1304 W. Green St., Urbana, IL 61801, USA. E-mail: sdillon@illinois.edu

† Electronic supplementary information (ESI) available: Fig. S1–S3 and Video S1. See DOI: 10.1039/c3cc46737f

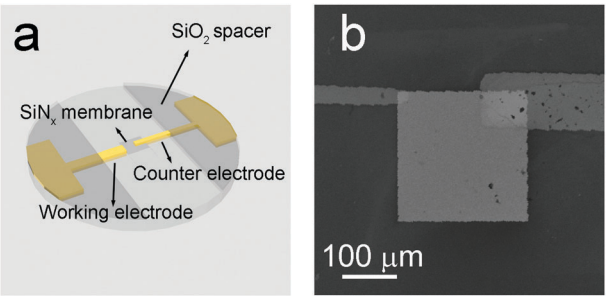

Fig. 1 (a) Schematic of the SiN_x grid utilized for assembling the *in situ* environmental cell. (b) SEM image of the 50 nm SiN_x window patterned with gold electrodes, used in this study, imaged after testing.

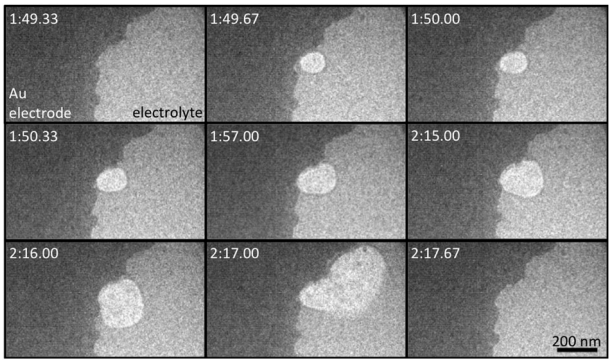

Fig. 2 Time-lapse TEM images depicting nucleation and growth of electrolytic gas at the gold electrode.

gas at electrodes on relatively short time scales. This work characterizes phenomenology associated with electrolytic gas nucleation and growth.

25 nm Au electrodes were patterned on commercial silicon supported amorphous silicon nitride (SiN_x) windows using photolithography. A 5 nm Cr adhesion layer ensured adhesion between the film and substrate. Patterned Cr/Au films were also evaporated onto the backside of the grids to serve as bonding pads for Au microwire leads that connected to the external circuit. A 100 nm SiO_2 spacer was patterned around the SiN_x windows using electron beam evaporation. Fig. 1 shows the testing configuration of the biasing chip. Prior to the assembling the environmental cell, the SiN_x windows were made hydrophilic by plasma treatment. A droplet of 0.1 M H_2SO_4 solution was applied to the top surface of the biasing chip. A second blank SiN_x chip was placed on top enclosing the liquid electrolyte. The microscale electrochemical cell was sealed *via* three O-rings in an environmental cell described in detail elsewhere.[11] Due to the compliance of the SiN_x windows the sample thickness may vary with position, however for current experiments the thickness was ~300–500 nm. The samples were imaged at a beam current density <1 A m^{-2} in a JEOL 2010LaB$_b$ TEM. Below this value of current density, it is difficult to routinely obtain an accurate measurement in our system. However, beam induced gas production is negligible on the experimental timescales below 40 A m^{-2} and no beam induced gas was observed in our system for over 30 min of exposure to the beam current density used for the experiments. Electrolysis was performed at voltages ranging from -1.6 V to -2 V.

At potentials up to -1.9 V, no electrolytic gas was observed on the time scale of 10 min. One potential challenge associated with *in situ* TEM relates to the fact that small areas are probed in a single experiment and that the reaction of interest may be localized outside of the region observed if it is sufficiently sparse or infrequent. At -2 V, the nucleation and growth of electrolytic gas was observed at the cathode (see Fig. 2 and Video S1, ESI†). The current response may be seen in Fig. S1 (ESI†). The voltage for generating electrolytic gas in the environmental cell was larger than the -1.6 V threshold voltage for the bulk system which was obtained from *ex situ* tests using the same chemistry. This is consistent with prior studies that cite a higher threshold voltage necessary to initiate electrolysis in an electrochemical microcell.[5] The gas evolved should be primarily H_2 based on solution chemistry and the fact that water vapour would be negligible in the bubble at the internal pressures associated with nanoscale bubbles. The video was captured at 3 frames per second. The formation and initial coarsening of a critical nuclei occur at a rate too rapid to capture with our detector.[5] The projected area of the bubble observed in the first frame at 226 s is 9800 nm^2 and the uniform image intensity variation across the bubble suggests that it spans the entire thickness of the cell (volume $\sim 5 \times 10^6$ nm^3).

The interesting feature of the bubble at the initial stage observed is that it is isolated from the electrode by a thin, 6–8 nm, layer of solution. The result suggests that the bubble nucleated homogeneously near the electrode interface (see Fig. S2, ESI†). Such nucleation has been predicted to occur at electrodes that are poorly wetted by the gas phase. It is possible that nucleation occurred heterogeneously at the window away from the electrode interface. However, this still supports the idea that hydrogen molecules initially dissolve into solution and subsequently precipitate out, and that the nucleation may be favorable in the electrical double layer or regions with steep composition gradients. Given the temporal resolution it is difficult to distinguish the center of mass of the critical nuclei. The fact that the bubble subsequently wets the electrode, in a thermodynamically irreversible interaction, indicates that the bubble could not have initially formed on the electrode surface. The bubble is stable in this position for ~2 s prior to wetting the electrode. Nucleation occurred adjacent to a concave region of the gold surface, which is consistent with the generally held belief that bubbles preferentially nucleate at surface cavities, scratches, and fissures where the solubility is highest due to the Gibbs–Thompson effect.[12]

Fig. 3a plots the projected area of the bubble as a function of time. The bubble area initially increases rapidly and decelerates to a linear growth rate that persists for ~20 s. Unlike results of prior studies characterizing individual micron scale bubbles,[12] the early stage of bubble coarsening observed here does not correlate with a simple growth exponent that can be rationalized on the basis of a particular rate limiting mechanism.[13] Assuming ideal gas behaviour, the pressure inside the bubble could be estimated following the Laplace–Young equation, $P = P_o + \gamma\kappa$, where γ is the surface tension of the liquid–vapour interface, P is pressure, and κ is the mean curvature of the bubble. The large excess

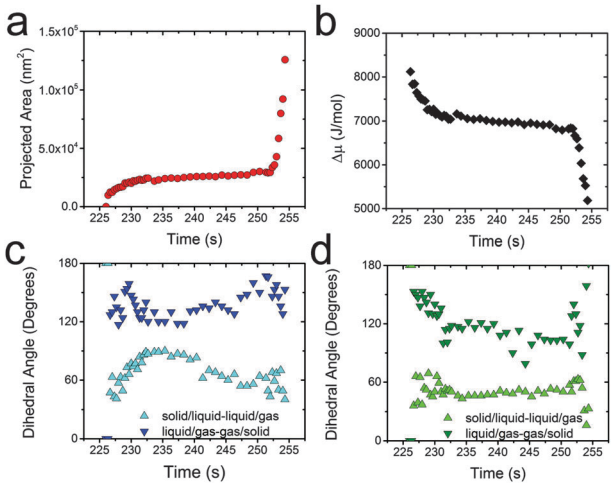

Fig. 3 (a) Time-dependent evolution of the projected area of the bubble, (b) calculated chemical potential difference between H_2 in the bubble and in solution, (c) the dihedral angles associated with the lower triple line, and (d) the dihedral angles associated with the upper triple line.

pressure associated with the curvature of the bubble produces a chemical potential difference between the gas in the bubble and the solution equilibrated with a flat surface (see Fig. 2b). The reduction in the rate of bubble growth and the rate of decreasing chemical potential correlates with the impingement of the triple lines at asperities on the Au surface. We hypothesize that the decrease in bubble coarsening at this point is associated with the barrier imposed by forming non-equilibrium dihedral angles and introducing excess curvature into the bubble in the process. Prior computational studies also indicate that triple line pinning inhibits bubble motion.[14] The growth rate subsequently accelerates until the bubble detaches from the electrode. Instead, we hypothesize that movement of the electrode–solution–gas triple phase boundary across asperities on the rough electrode surface thermodynamically limits coarsening of nanoscale bubbles. Fig. 3c and d plot the dihedral angles between the electrode and the solution–gas interfaces (see Fig. S3 for details, ESI†). The bubble initially coarsens rapidly as it wets the concave portion of the surface. The dihedral angles also vary rapidly, which is commonly associated with the stick–slip nature of their motion.[3,15] The growth slows when both triple lines reach a critical point that requires the bubble to envelope convex surface asperities. The bubble continues to coarsen slowly, taking on non-equilibrium dihedral angles, which also vary slowly. At ~250 s, the bubble expands rapidly normal to the electrode surface, destabilizing one of the triple lines and allowing it to wet along the surface. The bubble ultimately dewets the electrode and flows rapidly away. The process of bubble transport has been treated elsewhere with broader statistics and has similarly been associated with wetting instabilities.[16] Prior work has also found that surface significantly affects bubble motion.[17] By 900 s almost the entire window region (250 × 250 μm) is covered by evolved gas.

This work characterized the evolution of electrolytically generated H_2 using *in situ* TEM. The results demonstrate the fact that gas initially dissolves into solution and subsequently nucleates near Au electrodes, but not directly on their surface. The bubbles eventually wet the surface and their growth kinetics are strongly influenced by the surface roughness, which impacts the local dihedral angle and capillarity. Dewetting appears to be driven by a wetting instability.

This material is based upon work supported by the National Science Foundation under Grant No. 1254406.

Notes and references

1 L. Janssen, *Electrochim. Acta*, 1989, **34**, 161–169; R. Alkire and P. Y. Lu, *J. Electrochem. Soc.*, 1979, **126**, 2118–2124.
2 K. V. Dapkus and P. J. Sides, *J. Colloid Interface Sci.*, 1986, **111**, 133–151.
3 S. Lubetkin, *Electrochim. Acta*, 2002, **48**, 357–375.
4 C. A. Sequeira, D. M. Santos, B. Šljukić and L. Amaral, *Braz. J. Phys.*, 2013, 1–10; H. Vogt, *Electrochim. Acta*, 1984, **29**, 167–173.
5 V. B. Svetovoy, R. G. Sanders and M. C. Elwenspoek, *J. Phys.: Condens. Matter*, 2013, **25**, 184002.
6 L. Zhang, Y. Zhang, X. Zhang, Z. Li, G. Shen, M. Ye, C. Fan, H. Fang and J. Hu, *Langmuir*, 2006, **22**, 8109–8113.
7 S. Shibata, *Bull. Chem. Soc. Jpn.*, 1963, **36**, 53–57.
8 H. Vogt, *Electrochim. Acta*, 1978, **23**, 203–205; K. Stephan and H. Vogt, *Electrochim. Acta*, 1979, **24**, 11–18; S. A. Guelcher, Y. E. Solomentsev, P. J. Sides and J. L. Anderson, *J. Electrochem. Soc.*, 1998, **145**, 1848–1855.
9 N. de Jonge and F. M. Ross, *Nat. Nanotechnol.*, 2011, **6**, 695–704; E. R. White, M. Mecklenburg, S. B. Singer, S. Aloni and B. C. Regan, *Appl. Phys. Express*, 2011, **4**, 055201.
10 K. W. Noh, Y. Liu, L. Sun and S. J. Dillon, *Ultramicroscopy*, 2012, **116**, 34–38; T. J. Woehl, K. L. Jungjohann, J. E. Evans, I. Arslan, W. D. Ristenpart and N. D. Browning, *Ultramicroscopy*, 2012, **127**, 53–63; Y. Liu, K. Tai and S. J. Dillon, *Chem. Mater.*, 2013, **25**, 2927–2933.
11 Y. Liu, X. Chen, K. W. Noh and S. J. Dillon, *Nanotechnology*, 2012, **23**, 385302.
12 J. Glas and J. Westwater, *Int. J. Heat Mass Transfer*, 1964, **7**, 1427–1443.
13 S. D. Lubetkin, *Chem. Soc. Rev.*, 1995, **24**, 243–250.
14 J. H. Weijs and D. Lohse, *Phys. Rev. Lett.*, 2013, **110**, 054501; Y. Liu and X. Zhang, *J. Chem. Phys.*, 2013, **138**, 014706.
15 D. E. Westerheide and J. Westwater, *AIChE J.*, 1961, **7**, 357–362.
16 B. Kabanov and A. Frumkin, *Zh. Fiz. Khim.*, 1933, **4**, 539.
17 E. Dussan, *J. Fluid Mech.*, 1985, **151**, 1–20; E. Dussan and R. T.-P. Chow, *J. Fluid Mech.*, 1983, **137**, 1–29.